Renewable Energy 256 (2026) 124295

Contents lists available at ScienceDirect

Renewable Energy

journal homepage: www.elsevier.com/locate/renene

Effect of titanium-based supports on the electrochemical activity and stability of iridium nanoparticle catalysts for OER in PEM water electrolyzer

Lucinda Blanco-Redondo [a], Yevheniia Lobko [a,*], Alina Madalina Darabut [a], Jaroslava Nováková [a], Thu Ngan Dinhová [a], Maryna Vorokhta [b], Miquel Gamón Rodríguez [a], Milan Dopita [c], Michal Mazur [d], Jakub Hraníček [e], Yurii Yakovlev [a], Tomáš Hrbek [a], Vladimír Matolín [a], Iva Matolínová [a]

[a] Department of Surface and Plasma Science, Faculty of Mathematics and Physics, Charles University, V Holešovičkach 2 Prague 8, 180 00, Czech Republic
[b] Geochemistry Department, Institute of Rock Structure and Mechanics, The Czech Academy of Science, V Holešovičkách 94 Prague 8, 182 09, Czech Republic
[c] Department of Condensed Matter Physics, Faculty of Mathematics and Physics, Charles University, Ke Karlovu 5 Prague 2, 121 16, Czech Republic
[d] Department of Physical and Macromolecular Chemistry, Faculty of Science, Charles University, Hlavova 8 Prague 2, 128 00, Czech Republic
[e] Department of Analytical Chemistry, Faculty of Science, Charles University, Hlavova 2030/8 Prague 2, 128 00, Czech Republic

ARTICLE INFO

Keywords:
Iridium nanoparticles
Oxygen evolution reaction
Titanium
Degradation processes
Water electrolyzer

ABSTRACT

Efficient and stable oxygen evolution reaction catalysts are essential for advancing hydrogen production through water electrolysis. This study investigates the role of titanium-based supports — TiO_2, TiC, and TiN — in enhancing the activity and stability of iridium (Ir) nanoparticles, focusing on their morphological, chemical, and electrochemical properties. In a half-electrochemical cell, iridium supported on titanium dioxide (Ir/TiO_2) and titanium carbide (Ir/TiC) exhibited excellent OER performance with an overpotential of 260 mV and 259 mV at 10 mA cm^{-2}, respectively, which are comparable to unsupported Ir black nanoparticles (253 mV). In contrast, Ir supported on titanium nitride (Ir/TiN) showed a higher overpotential of 329 mV. The catalytic performance of these materials was further evaluated in a single-cell proton exchange membrane water electrolyzer. Post-mortem analyses of the membrane electrode assemblies revealed support-specific degradation pathways, including oxidation and dissolution processes. The findings highlight the influence of support material properties — such as conductivity, crystallinity, and composition — on the efficiency and durability of Ir nanoparticles. These insights provide a valuable foundation for designing advanced catalytic materials for water electrolyzers.

1. Introduction

To attain international climate and energy goals for net-zero greenhouse gas emissions, green hydrogen produced from renewable electricity is essential as a feedstock, fuel, and energy carrier [1]. Proton exchange membrane water electrolysis (PEMWE) offers an efficient pathway for green hydrogen production. This process relies on iridium-based catalysts for the oxygen evolution reaction (OER) occurring at the water electrolyzer anode due to its balanced catalytic activity and stability under the acidic, high-potential conditions of the OER [2]. However, the scarcity and high cost of iridium present a major obstacle to scaling up hydrogen technology. Reducing the Ir loading in PEMWE cells from the current standard of 3 mg cm^{-2} to 0.50 mg cm^{-2} is a key target for overcoming this challenge [3].

To optimize the catalyst usage while reducing metal loading and maintaining cell performance, several strategies have been developed. These include the design and production of core-shell structures [4], nanofibers [5], sputtered thin films [6], and single-atom catalysts [7]. Nevertheless, these methods face limitations in large-scale production due to their complexity. An alternative approach involves dispersing iridium nanoparticles on low-cost support materials that are stable in acidic media under high potential. In addition, these support materials should promote uniform distribution of catalytic nanoparticles, prevent agglomeration, maintain a high surface-to-bulk ratio, and optimize electron conductivity.

Metal oxides such as titanium dioxide (TiO_2) and tin oxide (SnO_2)

* Corresponding author.
E-mail address: yevheniia.lobko@mff.cuni.cz (Y. Lobko).

https://doi.org/10.1016/j.renene.2025.124295
Received 6 January 2025; Received in revised form 2 August 2025; Accepted 19 August 2025
Available online 1 September 2025

have emerged as promising support alternatives due to their chemical, electrochemical, and thermal stability [8]. However, their low electron conductivity can impede catalyst performance. Consequently, the catalyst loading has to be increased to form a conductive film that prevents the high electron resistance, bringing again the problem of the high catalyst loading [9].

The mechanism of charge transfer in TiO_2 can be complex and depends on its structural and electronic properties. As previously reported [10], charge transport may proceed via several regimes, including hole tunneling through a thin insulating oxide layer, state-mediated hole transport, or conduction via the valence band edge. These limitations have driven research towards modified oxide supports with improved conductivity. One potential solution to address the electron conductivity limitations of TiO_2 consists of using substoichiometric oxides such as the Magnéli phase Ti_4O_7 [11], which has oxygen vacancies that create electron pathways. Recent studies have investigated the effect of Ti_4O_7 on iridium kinetics and, even though the results are promising, the actual metal-support interaction is complicated to elucidate [12]. Another approach for improving the metal oxide conductivities involves doping with heteroatoms, such as Nb-TiO_2 [13], $W_xTi_{1-x}O_2$ [14], and Sb-SnO_2 [15]. These doped materials offer additional benefits, including an increased specific surface area for better Ir nanoparticle dispersion, the introduction of redox couples for additional capacitance, or active participation in the OER. A different strategy for increasing the conductivity, as well as improved catalyst stability, involves carbon-containing materials, such as carbon nanotube (CN@TiO_2) [16] or nitrogen-doped graphene-titanium dioxide composite (N-Graphene@TiO_2) [17]. Alternatively, Ti-based nanoparticles like titanium carbide (TiC) and titanium nitride (TiN) can address the conductivity challenges. Titanium carbide is a strong candidate due to its excellent electron conductivity, though it may suffer carbon losses at high potentials [18]. On the other hand, titanium nitride has shown outstanding results in terms of activity and stability compared to unsupported catalysts [19], and titanium oxynitride (Ti-O_x-N_y) has demonstrated remarkable stability due to its enhanced metal-support interaction [20].

This study focuses on using three different Ti-based nanoparticles — TiO_2, TiC, and TiN — as supports for synthesizing catalytically active Ir nanoparticles. The structural and chemical properties of the prepared catalysts have been analyzed to understand the impact of the support material on the OER activity of the iridium nanoparticles. Finally, a comparative analysis of the catalyst activity was conducted using a single-cell PEMWE under real operating conditions, followed by a post-mortem analysis of the membrane electrode assemblies (MEAs). This analysis reveals the different degradation pathways for each catalyst and helps to identify the material properties critical for developing more efficient and durable catalysts.

2. Materials and methodology

2.1. Chemical and materials

The metal precursor dihydrogen hexachloroiridate (IV) hydrate ($H_2IrCl_6{\cdot}xH_2O$ 99.99 %) and ethylene glycol (99 %) were acquired from Alfa Aesar and used as received. TiO_2 was purchased from Merck, and TiC and TiN powders from US Research Nanomaterials. Nafion perfluorinated resin 5 w/w% in alcohol/H_2O was purchased from the Fuel Cell Store. Ultrapure sulfuric acid (H_2SO_4, 95.0–97.0 %) for electrochemical measurements was obtained from Honeywell Fluka. Isopropanol (p.a.) was acquired from Penta. The water used in all tests was ultrapure (Millipore, 18.2 MΩ cm).

2.2. Synthesis of catalysts

Iridium on Ti-based nanoparticles was prepared by the polyol method. First, 346 mg of each support (TiO_2, TiC, or TiN) was dispersed in 275 ml of polyethylene glycol in a 500 ml round flask. Then, the mixture was heated up to 160 °C using a stirring heating mantle (Witeg). Once the set point temperature was reached, 25 ml of polyethylene glycol containing 30.9 mg of iridium salt $H_2IrCl_6{\cdot}xH_2O$ was added in a single dose with vigorous stirring. The concentration of the Ir salt in the total solution was 0.002 M. The Ir reduction was carried out for 1 h at 160 °C under constant stirring. Next, the nanoparticle suspension was naturally cooled down to room temperature and centrifuged at 6000 rpm for 15 min. Finally, the solid fraction obtained was rinsed with isopropanol to eliminate any traces of the solvent and again centrifugated. The cleaning procedure was repeated three times with isopropanol and a fourth time using water. Ultimately, the samples were dried overnight in an oven set to 50 °C. Three samples were prepared using the process described above: Ir/TiO_2, Ir/TiC, and Ir/TiN, with reaction yields of 93 %, 95 %, and 94 %, respectively.

2.3. Physicochemical characterization

The elemental chemical composition was evaluated by two techniques: the energy dispersive X-ray spectroscopy (EDX) and the inductively coupled plasma mass spectrometry (ICP-MS). The EDX analysis was performed at accelerating voltages of 20 kV using a Tescan MIRA 3 scanning electron microscope (SEM) equipped with a Bruker Quantax detector XFlash 6|10 spectrometer. To perform ICP-MS measurements, the digestion of the catalysts was done by wet acid treatment, consisting of a concentrated mixture of HCl:H_2O_2 (1:1) (Penta) for the Ir digestion, followed by the addition of $(NH_4)_2SO_4/H_2SO_4$ at 250 °C under stirring for Ti-containing compound digestion. The ICP-MS measurements were performed using an inductively coupled plasma mass spectrometer ICP-MS 7900 (Agilent, USA) equipped with a micromist glass nebulizer working at 1550 W (with a flow of 1.03, 0.90, and 15.0 dm3 min−1 of nebulizer, auxiliary, and plasma gas, respectively). Results were evaluated from the "No gas" mode for ^{193}Ir (62.7 % of natural abundance) and ^{47}Ti (7.44 % of natural abundance) isotopes. As an internal standard, ^{209}Bi was used for both isotopes. For calibration and sample solutions preparation, a 5 % (*v/v*) water solution of H_2O_2:HCl (1:1) (Penta) was used. Working standards were prepared by an appropriate diluting of one multielement certified reference solution AN9087MC (Au, Ir, Os, Pd, Pt, Rh, Ru) with a concentration of 100 mg dm^{-3} of each element in 20 % HCl and one single element certified reference solution AN8061FN (Ti) with a concentration of 100 mg dm^{-3} (both Analytika, Czech Republic). The concentrations of both elements in the calibration solutions were in a concentration range of 0.0016–5.0 mg dm^{-3}.

The micropore and mesopore parameters of samples were determined from the N_2 sorption isotherms measured at the liquid nitrogen boiling temperature (−196 °C) using a SURFER volumetric sorption analyzer (Thermo Fisher Scientific). Before the measurements, the samples were degassed at 75 °C for at least 12 h under a vacuum using a turbo pump. A burette with a volume of 10 cm^3 was used. The NPLT (Next Point Logarithm Triangulation) mode was set for all measurements as it automatically calculates the values at which the experimental isotherm points are collected. The equilibrium time for each isotherm point was 90 s, during which the deviation range was monitored to ensure it remained within the specified limits. If adsorption caused the deviation range to be exceeded, the equilibration time was extended until stable adsorption was achieved within the range for 90 s. At each measurement point, set pressures and temperatures were maintained with accuracies of ±0.15 % and ±0.01 °C, respectively. The saturation pressure of ±755 torr was controlled using atmospheric pressure monitoring during the experiment with a resolution of 0.1 torr. Blank helium was performed at −196 °C for all samples, as their skeletal density was unknown. The measured N_2 adsorption isotherms were fitted with the Brunauer-Emmett-Teller (BET) equation in the relative pressure range of p/p_s = 0.05–0.3 to calculate the BET specific surface area (SSA). The pore size analysis over the complete micro and mesopore size range was determined by the Non-Local Density Functional Theory (NLDFT) model applied to the physical adsorption of nitrogen

over the range of pore size between 0.5 and 30 nm using SAIEUS software (Micromeritics).

The catalysts' morphology and structure were characterized by employing transmission electron microscopy (TEM) in high-resolution mode (HR-TEM), using a JEOL 2200FS microscope and in high-angle annular dark field (HAADF) scanning mode (STEM) using JEOL NEOARM-200F microscope, both operating at an accelerated voltage of 200 kV. The composition of the catalyst was analyzed by EDX spectroscopy, complemented by TEM, using the JEOL JED-2300 energy dispersive X-ray analyzer. Specimens were prepared by placing a drop of the catalyst dispersion in isopropyl alcohol on a 300-mesh copper grid covered by a lacey carbon film (Agar Scientific). X-ray diffraction (XRD) patterns were recorded using a Rigaku SmartLab diffractometer equipped with a 9 kW Cu rotating anode, equipped with Johansson monochromator, wavelength (λ = 1.54059 Å), variable slits optics and a HyPix3000 detector. The measurements were completed in the angular 2Θ range from 10° to 150° in reflection, parafocusing Bragg-Brentano geometry. Measured diffraction patterns were fitted using the whole powder pattern fitting method (Rietveld method) using the software MStruct. Small-angle X-ray scattering (SAXS) measurements were performed with a Xenocs Xeuss 2.0 instrument equipped with a Mo Kα microfocus X-ray source ($\lambda = 0.7108$ Å), a paraboloid multilayered X-ray mirror, producing a parallel beam, two sets of scatter-less slits, and a Dectris Pilatus 200k, hybrid pixel single photon counting, detector. The experiments were performed at a detector distance of 2.5 m to cover the maximum accessible Q-range. Measured 2D intensity profiles were azimuthally integrated. The resulting 1D SAXS patterns were corrected to the sample thickness, the transmission of samples, and the adequately scaled signal from a Kapton sample holder was subtracted. SAXS patterns were fitted with a sphere@hardsphere model using the SasView software.

Electrical resistance was measured using both four-point probes (for low resistance) and two-point probes (for high resistance) techniques with an SP-150-1 potentiostat (BioLogic Science Instruments, France). The samples were prepared in the form of pellets (diameter 1.6 cm) by pressing the material under a pressure of 90 kN using a hydraulic press (H-62, Trystom).

The surface chemical composition of the nanoparticles was analyzed by X-ray photoelectron spectroscopy (XPS). The samples were studied in a powder form and as a catalyst layer deposited on a Nafion membrane after testing in a PEMWE single cell. In both cases, the samples were glued onto a carbon tape, which was fixed on a stainless-steel sample holder. The measurements were performed in an EnviroESCA device (Electron Spectroscopy for Chemical Analysis Under Environmental Conditions) from SPECS GmbH group (Germany) with a monochromated micro-focused Al Kα X-ray source (1486.71 eV). The device is equipped with a hemispherical photoelectron analyzer Phoibos 150 NAP 1D-DLD64 (SPECS), and the signal detection was done in FAT (Fixed Analyzer Transmission) under a pressure of 10^{-7} mbar. The spot size was 200 μm. The spectra of the core levels Ir 4f, Ti 2p, C1s, N 1s, O 1s, and F 1s were recorded with a resolution of 0.1 eV, dwell time of 0.3 s, and pass energy of 20 eV. The collected data was processed using KolXPD software. No shifting corrections were necessary, and the spectra were fitted as recorded. All fittings used a Shirley background. The Ir 4f core level was deconvoluted with several doublets corresponding to the number of chemical states found. An asymmetric Doniach–Sunjic function with a Gaussian profile was used for the doublets fitting. The branching ratio for the Ir 4f doublets was constrained to 4:3 and a binding energy splitting of 3 eV. The Ti 2p core level consisted of doublets fitted using two Voigt profiles with spin-orbit component splitting of 5.7 eV for Ti-O species and 6 eV for Ti-C, Ti-N, and Ti-O_x-N_y species. The amplitude of the $Ti2p_{1/2}$ peak was half the one for $Ti2p_{3/2}$, and a Gaussian width (g_{wid}) for $Ti2p_{1/2}$ was twice the one for $Ti2p_{3/2}$. A normalization by cross sections of 0.107 and 0.204 was applied to the Ti 2p and Ir 4f peak areas to calculate the ratio between XPS core levels.

2.4. Electrochemical measurements

2.4.1. Working electrode preparation

The working electrode consisted of a gold disc (Pine Research Instrumentation) of 5 mm diameter. The catalyst ink and its deposition were done following reference [21].

2.4.2. Rotating disk electrode measurements

The electrochemical characterization of the nanoparticles was carried out by the rotating disk electrode (RDE) technique in a three-electrode setup from Pine Research Instrumentation. A platinum counter electrode (AFCTR5) and a standard Hg/Hg_2SO_4 reference electrode (Monokrystaly, RME 122 type) were used. The working electrode consisted of a gold disk coated by a layer of catalyst ink with a total catalyst loading of 0.204 mg cm^{-2}. All the experiments were conducted on an aqueous H_2SO_4 solution (0.5 mol L^{-1}) electrolyte at room temperature using a Bio-Logic SP-50 potentiostat. The potentials reported in this work are presented versus the reversible hydrogen electrode (RHE). The first measurement consisted of the fingerprint of the sample, recorded by cycling 20 voltammograms between the potential of 0.06 V and 1.51 V with N_2-purged electrolyte (N_2 Linde, 99.9996) at a scan rate of 50 mV s^{-1} and rotation of 1600 rpm to avoid the accumulation of oxygen bubbles on the working electrode surface. Then, the catalyst activity towards OER was studied by sweeping the potential up to 1.8 V and back to 1.2 V. The measurements were done at a scan rate of 5 mV s^{-1}. The back and forward linear sweep voltammetry (LSV) was recorded five consecutive times to see the evolution of the catalyst activity. All data were corrected for *iR* potential drop, with *R* as the solution resistance. The data were normalized by the surface area of the working electrode (0.19625 cm^2) to obtain the current density values in the units of mA cm^{-2} or by the Ir loading on the working electrode to obtain the mass activity, MA_{OER} (mA g_{Ir}^{-1}). The overpotential η (mV) at 10 mA/cm^2 was used as a parameter to compare the OER catalytic activity among samples, including the Ir black nanoparticles (Fuel Cell Store) used as a reference. The LSV curves were used to determine the Tafel plot by representing the logarithm of the current density against the potential. After fitting the linear region of the Tafel plot, the Tafel slope was determined from equation $\eta = a + b\ log\ [j]$, with η being the overpotential in V, *a* the exchange current density, *j* the current density in mA cm^{-2}, and *b* the Tafel slope in mV dec^{-1}.

2.4.3. Membrane electrode assembly (MEA) preparation

The proton exchange membrane (PEM) consisted of a Nafion membrane NR 212, 50.8 μm thick from Chemours coated on the anode side with the synthesized catalysts by the Meyer Rod technique. The rod (Erichsen) had a wire coil with a diameter of 60 μm. The ink consisted of 25 mg of catalyst powder diluted in 130 μl of Nafion dispersion D-521 with 5 % w/w of the polymer in a mixture of water and 1-propanol (Sigma-Aldrich). The solution was kept under an ultrasonic bath for 30 min for uniform powder dispersion. The metal loading was controlled by the difference in mass before and after the catalyst deposition using a polypropylene substrate. All the samples were done to keep a total Ir loading of 0.3 mg cm^{-2}. The anode porous transport layer (PTL) was titanium felt (Mott) covered by a 50 nm Pt layer on both sides by magnetron sputtering for corrosion protection. As the cathode catalyst, a commercial gas diffusion electrode (GDE) consisting of platinum supported on a carbon paper (loading 0.5 mg cm^{-2}, 60 % Pt, FuelCell Store) was used.

2.4.4. Water electrolyzer measurements

The MEAs were pressed between two end plates with serpentine flow fields (Tandem) made from Ti and an active surface area of 4.62 cm^2. The single-cell PEMWE was tested at 80 °C by an SP-150 potentiostat (BioLogic). The testing protocol comprises three measurements: the IV curves for voltages from 1.3 V to 2 V (step 5 mV), PEIS (DC at 1.5 V, frequency range of 200 kHz–500 mHz), and the current response to the

voltage switching between 1.6 V and 1.7 V (5 min long steps, 3 h total duration). The whole protocol was repeated three times. Between each measurement, the cell was held at an open-circuit voltage.

The PEIS measurements were conducted at voltages of 1.35, 1.37, 1.39, 1.41, 1.43, 1.45, 1.47, 1.49, 1.51, and 1.53 V, covering a frequency range of 200 kHz–500 mHz with an excitation amplitude of 5 mV. The data obtained from these measurements were analyzed using Relaxis3 software. The behavior of the PEMWE is effectively represented by the Randles Equivalent Electrical Circuit, which we used for data fitting. Given that the cathode impedance was minimal across all samples except for Ir/TiC, it was disregarded for Ir/TiO_2, Ir/TiN, and Ir black, focusing solely on fitting the anodic contribution (Fig. S15a). For Ir/TiC, however, a full Randles circuit was applied (Fig. S15b). Here, R_1 represents the total ohmic resistance of the cell, connected in series with a parallel arrangement of the anodic (or both anodic and cathodic) charge transfer resistance R_2 and the constant phase element P.

3. Results and discussion

3.1. Physicochemical characterization of the samples before the electrochemical measurements

EDX analysis was done to investigate the chemical composition of the samples, with detailed spectra available in the Supplementary Information (Fig. S1). The atomic ratio between iridium and titanium (Ir/Ti) is 0.08 for Ir/TiO_2 and Ir/TiC, and 0.07 for Ir/TiN, indicating similar Ir content (Table S1). Alternatively, the ICP-MS technique was used to determine Ir loading. Results show Ir mass loadings of 19.9 wt% for Ir/TiO_2, 19.2 wt% for Ir/TiC, and 17.9 wt% for Ir/TiN, which are consistent for the three catalysts.

TEM measurements were used to analyze the morphology of Ti-based supports and the distribution and particle size of iridium nanoparticles (Fig. 1 and Figs. S2-S4). TEM micrographs in Fig. 1 display Ti-based nanoparticles uniformly decorated with Ir nanoparticles. The inserts in Fig. 1a–c shows an iridium mean particle size of 1.73 nm for Ir/TiO_2, 1.80 nm for Ir/TiC, and 1.48 nm for Ir/TiN. The mean particle sizes for TiO_2, TiC, and TiN supports are 26 nm, 31 nm, and 25 nm, respectively (Fig. S2d–f). Additionally, STEM imaging with corresponding EDX mapping of Ir/TiO_2 nanoparticles (Fig. 2) confirms the presence of Ir nanoparticles decorating the support. It is visualized as the overlay of elemental maps of Ir and Ti presented as green and red dots, respectively (Fig. 2b and c).

The Ir, TiO_2, TiC, and TiN nanoparticle crystallographic structures were verified using XRD analysis. Fig. 3a shows part of measured XRD patterns for the bare support nanoparticle and their corresponding Ir-decorated counterparts. TiO_2 exhibits reflections of two phases: anatase (88 wt%) and rutile (12 wt%). Both anatase (space group I 4_1/amd, - space group # 141) and rutile (space group P 4_2/mnm, - space group # 136) are of tetragonal structure. The refined lattice parameters of anatase TiO_2 are $a = 3.7851 \pm 0.0001$ Å and $c = 9.5046 \pm 0.0002$ Å, which aligns with tabulated data [22]. The main diffraction peaks for anatase TiO_2 appear at 2Θ of 25.3°, 37.8°, and 48.0°, corresponding to the (101), (004), and (200) planes, respectively (indicated by the asterisks in Fig. 3a). The mean size of coherently diffracting domains of anatase TiO_2 is 24 nm. For rutile TiO_2, the refined lattice parameters are $a = 4.5934 \pm 0.0001$ Å and $c = 2.9587 \pm 0.0001$ Å, also in agreement with tabulated data [22]. The mean size of coherently diffracting domains of rutile TiO_2 is 40 nm, with its primary diffraction peak at 2Θ of 27.4°, corresponding to the (110) plane (marked with a dot in Fig. 3a).

Both TiC and TiN crystallize in the face-centered cubic (fcc) structure (space group Fm $\bar{3}$ m, space group #-225), as shown in Fig. 3a. The refined lattice parameters are 4.3176 ± 0.0001 Å for TiC and 4.2386 ± 0.0001 Å for TiN, with mean crystal sizes of 33 nm and 35 nm, respectively. The most intensive diffraction peaks for TiC are observed at 2Θ values of 35.9° and 41.7°, corresponding to the (111) and (200) planes, respectively. Similarly, TiN shows main diffraction peaks are at 2Θ values of 36.6° and 42.5°, corresponding to the same reflection planes as TiC.

The XRD patterns of the supported Ir nanoparticles (Fig. 3a) shows no detectable Ir diffraction peaks at 2Θ values of 39.7° and 46.4° (indicated by solid bars at the bottom of Fig. 3a). This absence is consistent with the small sizes of the Ir nanoparticles, which are less than 2 nm (Fig. 1) [23], and the Ir loading, below 20 wt% [24]. STEM (Fig. S3) and HR-TEM (Fig. S4) images confirm the crystalline nature of the Ir nanoparticles. Further analysis of the line intensity profile (Fig. S4a–c) reveals interplanar distances of 2.3 Å and 1.9 Å, corresponding to the d-spacings of the (111) and (200) planes of iridium, respectively.

SAXS measurements were conducted to statistically analyze the size distribution of the Ir nanoparticles. As shown in Fig. 3b, the SAXS patterns confirm the presence of small Ir particles with an average size of approximately 1.7 nm, consistent with the TEM results. For reference, the SAXS patterns of the bare TiO_2, TiC, and TiN supports are provided in Fig. S5.

The specific surface area (SSA) of the nanoparticles was evaluated using the BET method, as illustrated in Fig. 4 (solid fill). Results show that TiO_2 has the highest SSA at 48.8 m^2/g, followed by TiN at 40.5 m^2/g, and TiC at 30.3 m^2/g. For TiC, an inverse relationship is observed between the SSA and the particle size, with TiC exhibiting the largest mean particle size (Fig. S2e) and the lowest SSA. In contrast, TiO_2 displays a higher SSA than TiN despite their similar mean particle sizes. This difference is attributed to variations in porosity, which contribute to the total surface area (Fig. 4, pattern fill). Smaller particles generally exhibit higher SSA due to their increased surface area-to-volume ratio. Additionally, TiO_2 has a greater pore volume (0.23 $cm^3\ g^{-1}$) compared to TiN (0.13 $cm^3\ g^{-1}$). After the deposition of Ir nanoparticles, all three

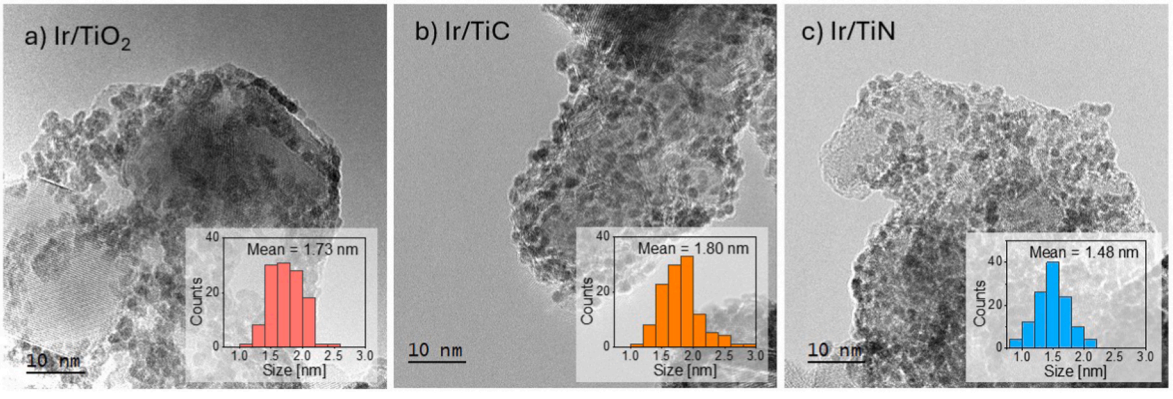

Fig. 1. TEM images of the supported Ir nanoparticles (a–c) and Ir particle size distribution (insets).

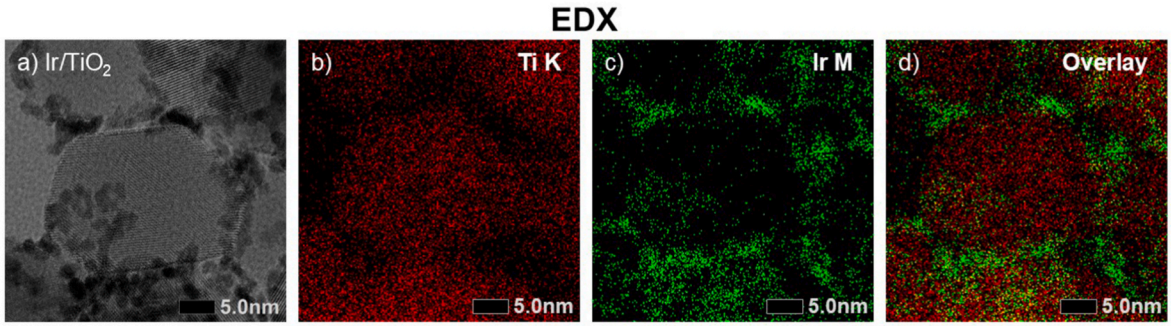

Fig. 2. HAADF-STEM image of Ir/TiO_2 (a), and corresponding EDX mapping (b–d). Color code: red (titanium), green (iridium). (For interpretation of the references to color in this figure legend, the reader is referred to the Web version of this article.)

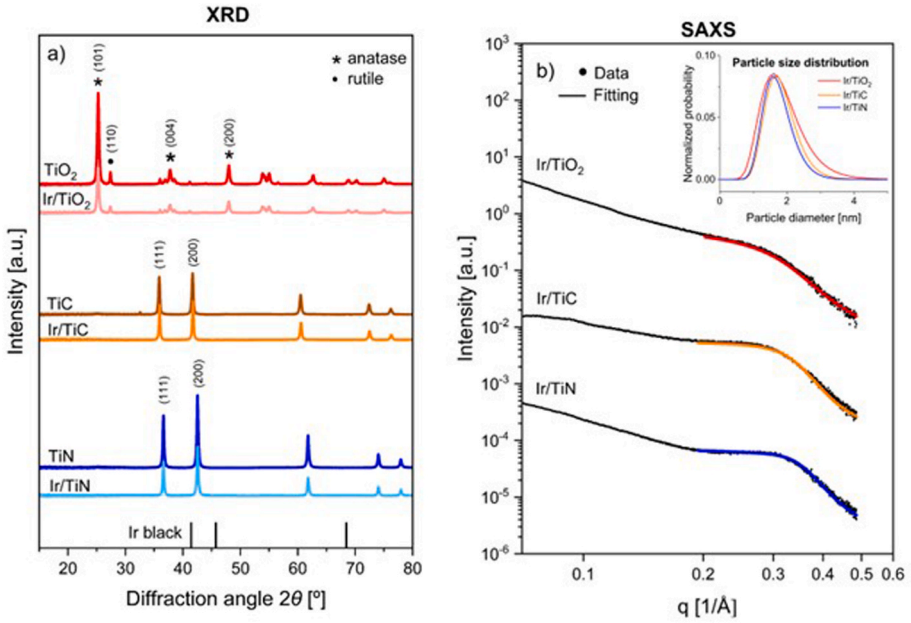

Fig. 3. XRD patterns of TiO_2, Ir/TiO_2, TiC, Ir/TiC, TiN, and Ir/TiN (a). Asterisks correspond to the anatase TiO_2 phase, dots to the rutile TiO_2 phase, and vertical bars on the bottom to the Ir diffraction peaks; SAXS patterns of Ir/TiO_2, Ir/TiC, and Ir/TiN, including data and fitting (b). The inset corresponds to the Ir particle size distribution.

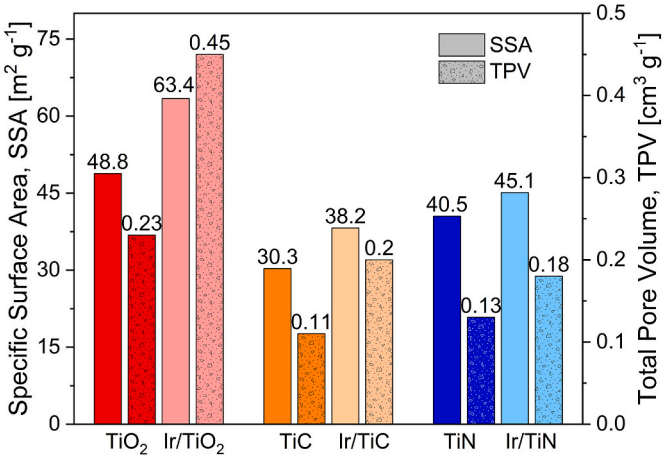

Fig. 4. Specific Surface Area (SSA, solid fill) and the Total Pore Volume (TPV, pattern fill) of the support nanoparticles (dark color) and the corresponding supported-Ir nanoparticles (light color). (For interpretation of the references to color in this figure legend, the reader is referred to the Web version of this article.)

Ir-decorated supports experienced increases in both SSA and pore volume. This change is likely due to the surface roughness and interfacial voids (nanoscale gaps or pores generated at the Ir-support interface as a result of particle clustering or incomplete surface coverage (lighter color columns). This positive impact on SSA and total pore volume highlights the effects of Ir deposition. However, variations in Ir loading and particle size across the titanium-based supports influenced the observed changes in surface properties. The SSA increases recorded were 14.6 m^2/g for Ir/TiO_2, 7.9 m^2/g for Ir/TiC, and 4.6 m^2/g for Ir/TiN, corresponding to deposited Ir amounts of 19.9 %, 19.2 %, and 17.9 %, respectively.

The surface chemical composition of the prepared catalysts was investigated using X-ray photoelectron spectroscopy (XPS). Fig. 5 presents the Ir 4f and Ti 2p core-level spectra for the support nanoparticles and their corresponding Ir-decorated versions. The Ir 4f spectra for Ir/TiO_2, Ir/TiC, and Ir/TiN (Fig. 5a) reveal two doublets: one at binding energies of 60.9 eV and 63.9 eV, corresponding to metallic iridium (Ir^0), and another at 61.8 eV and 64.8 eV, indicative of the Ir^{IV} oxidation state, associated with iridium dioxide (IrO_2) [25]. The ratio of metallic to oxidic iridium (Ir^0/Ir^{IV}) is 2.4 for Ir/TiO_2, 2.3 for Ir/TiC, and 1.7 for Ir/TiN. This suggests that the surface of the Ir nanoparticles is predominantly metallic (over 70 %) for both Ir/TiO_2 and Ir/TiC, and the percentage decreases to 62.7 % for Ir/TiN.

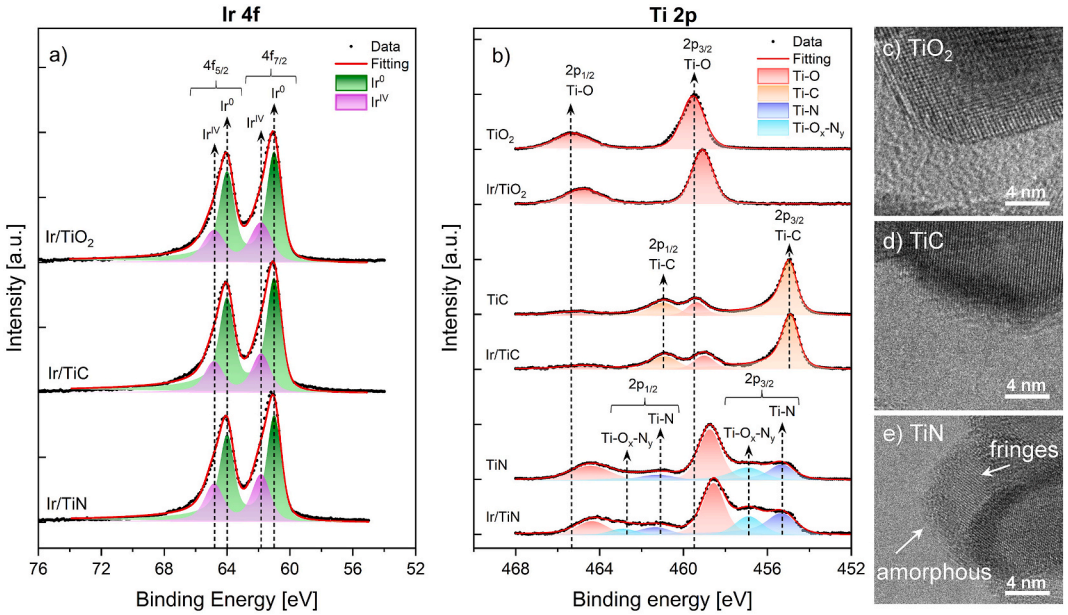

Fig. 5. XPS spectra of Ir 4f core level of Ir-decorated support powders (a), Ti 2p core level for non-decorated support and Ir-decorated support powders (b), and the HR-TEM micrographs of TiO_2 (c), TiC (d), and TiN (e).

For TiO_2 (Fig. 5b), the Ti 2p spectrum shows a single doublet with peaks at binding energies (BEs) of 459.5 eV and 465.3 eV, corresponding to the Ti $2p_{3/2}$ and Ti $2p_{1/2}$ spin-orbit splitting, respectively. These states are consistent with the presence of titanium in the TiO_2 chemical state [26], in agreement with the XRD data shown in Fig. 3a. In the Ir/TiO_2 spectrum, the Ti 2p doublet exhibits a 0.44 eV shift to lower BEs, potentially due to several factors. First, the effective electronegativity of the oxygen atoms in the Ti-O bonds may be reduced due to the redistribution of the electron density from the more electronegative iridium toward titanium, causing the observed shift. This redistribution, called the "titanium effect", was observed for metal-ceramic interfaces [27]. Additionally, the small size of the iridium nanoparticles (<2 nm) results in a high surface-to-volume ratio of atoms, increasing the proportion of undercoordinated surface sites and enhancing metal-support interactions [28].

For both TiC and Ir/TiC (Fig. 5b), the Ti 2p core-level spectra are deconvoluted into two distinct doublets, corresponding to titanium oxide (Ti-O) and titanium carbide (Ti-C) species. The Ti-O peaks in TiC are consistent with those observed for TiO_2 nanoparticles, and the Ti-C component exhibits peaks at binding energies of 454.9 eV for Ti $2p_{3/2}$ and 460.9 eV for Ti $2p_{1/2}$ [29]. In the Ir-decorated sample (Ir/TiC), the Ti-O component shifts by 0.37 eV to lower binding energies, while the Ti-C doublet remains unchanged compared to the bare TiC nanoparticles. This suggests that Ir interacts with Ti in the oxide state but not in the carbide state. The ratio of carbide-to-oxide species (Ti-C/Ti-O) is 4.2 for the TiC nanoparticles and slightly decreases to 3.5 after Ir deposition, indicating that the surface remains predominantly composed of Ti-C. Consequently, TiO_2 reflections are not visible in the XRD patterns of either TiC or Ir/TiC (Fig. 3a), as XRD cannot detect the thin titanium oxide layer present on the nanoparticle surface.

For both TiN and Ir/TiN nanoparticles (Fig. 5b), the Ti 2p core-level spectra are deconvoluted into three distinct doublets, corresponding to the nitride (Ti-N), oxynitride (Ti-O_x-N_y), and oxide (Ti-O) species [30]. The Ti $2p_{3/2}$ peak of the Ti-N component appears at a binding energy of 455.2 eV, the Ti-O_x-N_y species at 456.9 eV, and the Ti-O species at 458.6 eV. The spin-orbit splitting is 6.0 eV for the nitrogen-containing species and 5.7 eV for the oxide species. Notably, the Ti-O component in TiN exhibits a binding energy 0.8 eV lower than that observed for TiO_2 and TiC, aligning with values reported for amorphous TiO_2 occurring after air exposure of the material [31]. This shift suggests a difference in the oxide phase present on the TiN surface (amorphous TiO_2) compared to the phase detected in TiO_2 and TiC (crystalline TiO_2). The ratio of nitride to oxygen-containing species (Ti-N/(Ti-O_x-N_y + Ti-O)) is 0.3 for the bare TiN nanoparticles, increasing slightly to 0.4 after Ir deposition. In contrast to TiC nanoparticles, TiN has a higher oxide content on the surface, with more than 70 % of it composed of fully or partially oxidized titanium. Despite the increase in surface oxidation, no TiO_2 reflections are observed in the XRD patterns (Fig. 3a), confirming the amorphous nature of the surface oxide, which does not produce detectable diffraction peaks. Similar to the behavior observed in Ir/TiO_2 and Ir/TiC, the Ti-O component in Ir/TiN shows a 0.18 eV shift to lower binding energy after Ir deposition. At the same time, the binding energies of the Ti-O_x-N_y and Ti-N species remain unchanged upon Ir decoration. The differences in the crystalline and amorphous nature of the Ti-based supports are also evident in the HR-TEM micrographs shown in Fig. 5c–e. TiO_2 and TiC display distinct lattice fringes, sharp edges, and well-defined particle boundaries, indicating crystalline structure. In contrast, TiN shows clear crystal planes at the core of the particles, but blurred edges with short-range ordered patterns, which are characteristic of the amorphous TiO_2 phase [32].

3.2. *Electrochemical characterization*

Cyclic voltammetry (CV) was performed to investigate the electrochemical properties of the nanoparticles. Fig. 6 presents 20 consecutive cyclic voltammograms of the supported Ir nanoparticles, including Ir black as a reference for unsupported Ir. Continuous cycling was conducted to activate the Ir nanoparticles by inducing surface oxidation, forming hydrous Ir oxide [33]. In the low-potential region (0.06–0.4 V_{RHE}), peaks corresponding to hydrogen adsorption and desorption on metallic Ir sites are observed. Particularly, the peak in the anodic scan represents the hydrogen underpotential deposition (H_{upd}, Fig. S7).

For Ir/TiO_2 nanoparticles (Fig. 6a), a broad H_{upd} peak is observed, which disappears after the first cycle. This indicates that the Ir nanoparticle surface undergoes complete oxidation at higher potentials, making the hydrogen adsorption-desorption process ineffective due to the loss of metallic sites on the catalyst surface. In contrast, Ir/TiC nanoparticles (Fig. 6b) exhibit a sharper and more intense H_{upd} peak, representing more efficient hydrogen desorption. The different behavior of the H_{upd} peak between Ir/TiO_2 and Ir/TiC can be attributed to

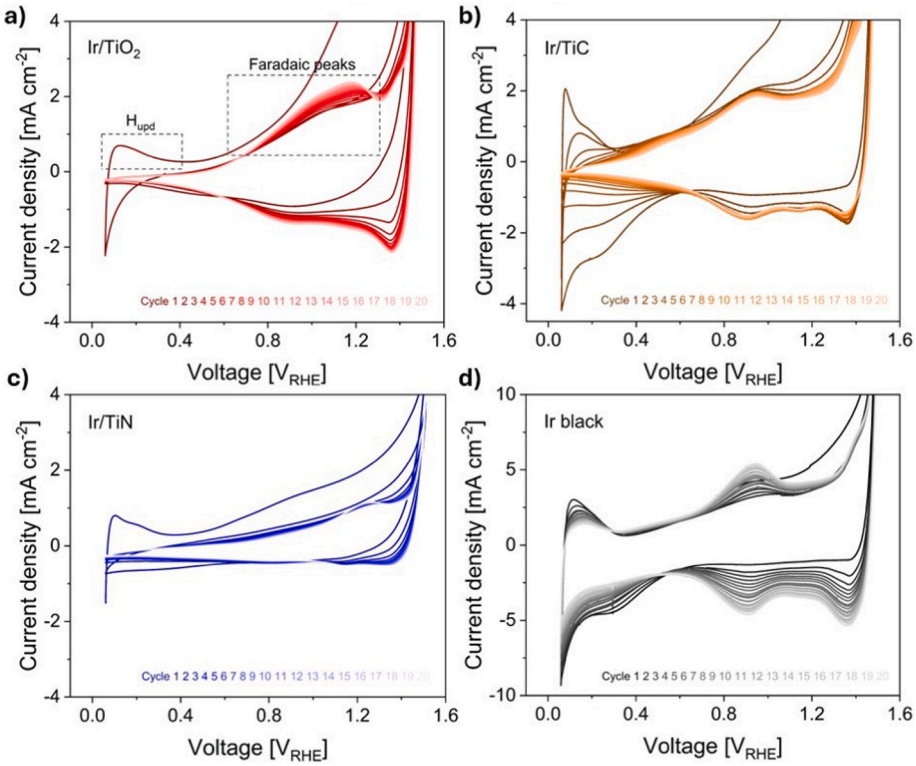

Fig. 6. Cyclic Voltammetry of Ir/TiO_2 (a), Ir/TiC (b), Ir/TiN (c), and Ir black (d) from cycles 1 to 20 in acidic electrolyte (0.5 M H_2SO_4), scan rate 50 mV s^{-1}, and potential range 0.051–1.56 V_{RHE}.

variations in the number of electrochemically active sites on the Ir surface induced by differences in the support electron conductivity. The TiO_2 nanoparticles have a lower electrical conductivity ($5.75{\cdot}10^{-9}$ S cm^{-1}, Table S2), which inhibits electronic transport, which may limit electron transfer between hydrogen and the Ir surface, which may limit electron transfer between hydrogen and the Ir surface, thereby reducing the effective number of electrochemically active sites. In contrast, TiC exhibits a high conductivity of 54.30 S cm^{-1} (Table S2), ensuring efficient charge transfer between the hydrogen and iridium atoms in the Ir/TiC catalyst. As a result, the Ir nanoparticles on TiC display more active sites compared to those on TiO_2, despite having similar structural and chemical properties, such as Ir loading on support, mean particle size (Fig. 1), and Ir chemical states (Fig. 5a). An additional difference between the Ir/TiO_2 and Ir/TiC nanoparticles is the evolution of the H_{upd} peak during continuous cycling. For Ir/TiC, the H_{upd} peak decreases gradually, suggesting a progressive oxidation of active sites. While for Ir/TiO_2, the peak disappears completely after just one cycle, indicating a more abrupt loss of accessible metallic Ir sites. The behavior is similar to that observed for Ir black (Fig. 6d).

The Ir/TiN nanoparticles exhibit a H_{upd} peak response comparable to Ir/TiO_2, characterized by low intensity and peak disappearance after one cycle. This response is unexpected given the conductivity of TiN nanoparticles (3.368 S cm^{-1}, Table S2), which is closer to the TiC conductivity – one order of magnitude lower – and significantly higher – nine orders of magnitude – than that of the TiO_2 nanoparticles. However, the conductive nature of TiN may be compromised by the formation of a surface oxide/oxynitride layer, as detected by XPS (Fig. 5b). Furthermore, the voltammetric response of the bare TiN nanoparticles (Fig. S8c) lacks any electrochemical features, despite the expected oxidation peak at 0.740 V_{RHE}, based on literature references [34]. The absence of an electrochemical signal aligns with the presence of an oxidized layer on the surface of the TiN nanoparticles, which also explains their semiconductor character similar to that of bare TiO_2 (Fig. S8a).

In the higher potential region (0.6–1.4 V vs. RHE), multiple faradaic peaks are observed during the cathodic scan. These reduction peaks correspond to sequential redox transitions of iridium oxide species, commonly attributed to Ir^{4+}/Ir^{3+} and Ir^{3+}/Ir^{0} couples, depending on the hydration state and crystallinity of the oxide layer. These peaks are further analyzed and quantified in terms of current density and charge evolution in Fig. 7 and Fig. S9. In terms of increasing faradaic charge (Fig. 7a), the Ir/TiO_2 nanoparticles display two faradaic peaks at 0.97 V_{RHE} and 1.18 V_{RHE} (Fig. S9a), with the total charge increasing 5.4-fold from 0.25 mC to 1.35 mC. Next, Ir black presents a single faradaic peak at 0.94 V_{RHE} (Fig. S9d), with a total charge increasing 4.3-fold from 0.50 mC to 2.17 mC. Ir/TiC nanoparticles show a faradaic peak at 0.94 V_{RHE} (Fig. S9b), which increases 2.08-fold from 0.25 mC to 0.52 mC. Finally, Ir/TiN nanoparticles exhibit a peak at 1.26 V_{RHE} (Fig. S9c), with the total charge increasing 1.2-fold from 0.07 mC to 0.16 mC.

While all samples exhibit an increase in faradaic charge, the most significant growth is observed for Ir/TiO_2 and Ir black, which is also reflected in the maximum current densities associated with these peaks (Fig. 7b). For Ir/TiO_2, the current density increases from 1.9 mA cm^{-2} to 2.4 mA cm^{-2}, while for Ir black, it increases from 3.3 mA cm^{-2} to 5.4 mA cm^{-2}. In contrast, the maximum current for Ir/TiN remains stable at around 1.1 mA cm^{-2} and decreases for Ir/TiC from 2.0 mA cm^{-2} to 1.8 mA cm^{-2}.

The peak evolution observed in Ir/TiO_2 and Ir black is produced by partially irreversible Ir oxidation, progressing from the surface to the bulk. This oxidation leads to the accumulation of redox sites, which are responsible for peak growth. In contrast, Ir/TiC and Ir/TiN exhibit a slight increase in the peak charge during the first five cycles as a consequence of the Ir surface oxidation. After the initial changes, both the charge and the peak currents stabilize, indicating no further oxidation.

The slowdown of the Ir activation for Ir/TiC and Ir/TiN nanoparticles might happen due to several reasons. In the case of Ir/TiC, oxidation of the TiC can occur preferentially to oxidation of the Ir. This is evident in

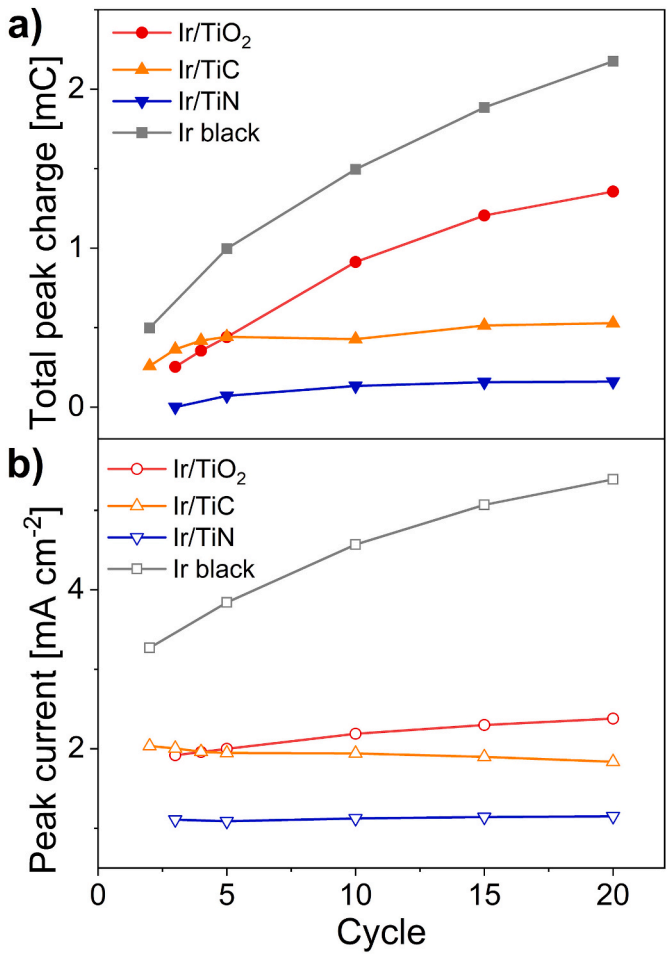

Fig. 7. Total peak charge (a) and peak current (b) for the faradaic peaks shown in Fig. 6 for Ir/TiO_2, Ir/TiC, Ir/TiN, and Ir black in the cycles between 2 and 20. The Ir loading on the working electrode is 0.04 mg cm^{-2} for Ir/TiO_2, Ir/TiC, and Ir/TiN and 0.20 mg cm^{-2} for Ir black.

the voltammetric response of bare TiC nanoparticles (Fig. S8b), which shows an oxidation peak at 1.16 V_{RHE} during the first anodic scan without a corresponding cathodic peak, indicating the irreversible passivation of the TiC surface [35]. Additionally, the increase in the TiC double-layer capacitance over cycles suggests ongoing surface changes in TiC linked to continuous oxidation. In the case of Ir/TiN, the low electrochemical response can be explained by the passivated nature of the TiN surface, consisting of amorphous TiO_2 and TiO_xN_y species (XPS in Fig. 5b), which could hinder charge transfer. Moreover, a relatively weak Ir-support interaction is indicated by a smaller Ti-O binding energy shift (0.18 eV) in comparison to the ones detected for Ir/TiO_2 (0.44 eV) and Ir/TiC (0.37 eV), suggesting less effective electronic coupling between Ir and the support.

3.3. Catalytic activity towards oxygen evolution reaction

To investigate the electrochemical activity of the nanoparticles towards the oxygen evolution reaction (OER), the potential in the half-cell was swept up to 1.8 V_{RHE}. The polarization curves, corrected for the *iR* potential drop, are presented in Fig. 8a. The Ir/TiO_2, Ir/TiC, and Ir black nanoparticles show comparable performance, while the Ir/TiN nanoparticles display lower current densities. To quantitatively assess the catalytic performance of each sample, key electrochemical parameters - such as the overpotential (η) at 10 mA cm^{-2}, the mass activity (MA) at 1.525 V_{RHE}, and the Tafel slope - were calculated and are presented in Fig. 8b.

Among the samples, the Ir/TiO_2 and Ir/TiC demonstrate a good OER efficiency, with overpotentials of 260 mV and 259 mV, respectively, which are close to the value observed for unsupported Ir black (253 mV). Comparable values were obtained by Lin et al. [12] for $IrTiO_x$ (296 mV), Han et al. [36] for IrO_x/TiN (293 mV), and Karade et al. [37] for IrO_2@Ir/TiN (232 mV). The worst result from the series presented in this work is obtained for the Ir nanoparticles supported on TiN, which required a higher overpotential of 329 mV to reach the target current density of 10 mA cm^{-2}. Similar overpotentials (η > 300 eV) have been reported in the literature for IrO_2-blue TiO_2 [38], IrO_x/Ti_4O_7 (3:7) [39], Ir/TiC [40], and IrO_2/TiN [41].

It is important to note that the electrochemical results obtained from experiments conducted in a half-cell can be strongly influenced by the iridium loading on the working electrode. In this context, mass activity (MA) is a more accurate parameter, as it normalizes the current density by the iridium mass. The Ir/TiO_2 outperforms the other samples in MA with 1298 mA g_{Ir}^{-1} (columns in Fig. 8b), followed closely by Ir/TiC (1173 mA g_{Ir}^{-1}). The Ir/TiN shows the lowest performance with 133 mA g_{Ir}^{-1}. Despite the good overpotential observed for Ir black, its MA is lower compared to the supported Ir nanoparticles due to the difference in loadings on the working electrode (0.20 mg cm^{-2} for Ir black vs 0.04 mg cm^{-2} for the supported samples). To gain perspective on these results, Fig. S10 presents the values of MA for Ir nanoparticles supported on

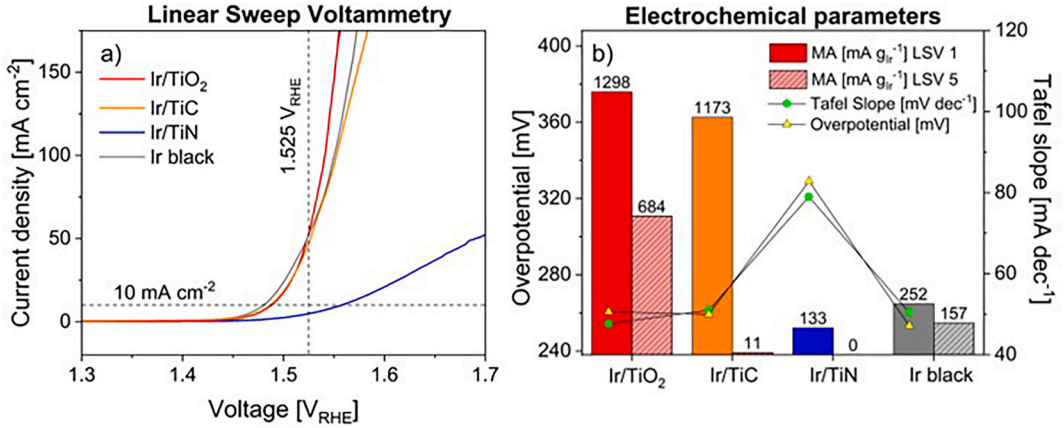

Fig. 8. *Ex situ* testing of Oxygen Evolution Reaction (OER): Linear Sweep Voltammetry (LSV) curves for Ir/TiO_2, Ir/TiC, Ir/TiN, and Ir black (a), and electrochemical parameters including overpotential (yellow triangles) at 10 mA cm^{-2}, Tafel slope derived from Tafel plot in Fig. S11 (green circles), and mass activity (MA) at 1.525 V_{RHE} for LSV 1 (solid column) and LSV 5 (lined column) (b). (For interpretation of the references to color in this figure legend, the reader is referred to the Web version of this article.)

TiO_2, TiC, and TiN reported over the last years, and the comparison demonstrates the improved activity shown by the Ir/TiO_2 and Ir/TiC nanoparticles presented in this work. For detailed information on the literature review, see Table S3.

The Tafel slope alone does not provide enough information to identify the rate-determining step of the reaction for each catalyst (green circles in Fig. 8b). However, the similar values of 47.7 mV dec^{-1} for Ir/TiO_2, 51 mV dec^{-1} for Ir/TiC, and 50.5 mV dec^{-1} for Ir black suggest that the OER proceeds by the same mechanism and that the presence of the support is not affecting the reaction pathway. In contrast, the Tafel slope of 79 mV dec^{-1} for Ir/TiN may indicate differences in the reaction mechanism. Some studies interpret higher Tafel slopes as indicative of poorer catalytic activity, corresponding to the higher overpotentials required to reach a specific current density. The Tafel plots and their linear fits are shown in Fig. S11.

Five consecutive linear sweep voltammetry (LSV) scans, recorded in both forward and backward directions, were conducted to investigate the evolution of catalyst activity over continuous cycling (Fig. S12). For Ir/TiO_2, the mass activity at 1.525 V_{RHE} decreases by 47 %, from 1298 mA g_{Ir}^{-1} to 684 mA g_{Ir}^{-1}. Ir black also shows a reduction in mass activity, with a 37 % decrease from 252 mA g_{Ir}^{-1} to 157 mA g_{Ir}^{-1}. The loss is more severe for Ir/TiC, dropping to 11 mA g_{Ir}^{-1}. For Ir/TiN, the current density reduces below 10 mA cm^{-2}, which impedes the determination of kinetic parameters (Fig. 8b, columns with lines). Table S4–S5 summarize the overpotential and mass activity values for each cycle. These results establish the order of catalytic performance, from highest to lowest, as Ir/TiO_2 > Ir black > Ir/TiC > Ir/TiN, in agreement with the degree of activation described by the growth of the faradaic peaks.

The catalytic behavior observed in the rotating disk electrode for each catalyst may differ under PEM water electrolyzer conditions. Therefore, each supported catalyst, along with pure Ir black as a reference, was deposited on a Nafion membrane and tested *in situ*. Fig. 9a shows the uncompensated current-voltage (IV) curves, and Fig. 9b shows the ohmic resistance for the four membrane electrode assemblies (MEAs): Ir/TiO_2, Ir/TiC, Ir/TiN, and Ir black. In the initial measurement (IV 1), Ir/TiO_2 exhibits superior catalytic activity, outperforming Ir black, Ir/TiC, and Ir/TiN. To reach a current density of 1 A cm^{-2}, Ir/TiO_2 requires the lowest potential (1.56 V), followed by Ir black (1.61 V), and Ir/TiC (1.85 V), while Ir/TiN fails to reach this current density. Notably, Ir/TiO_2 also surpasses other catalysts tested at low Ir loadings (0.1–0.5 mg cm^{-2}) [36,42–44] and shows a remarkable activity compared to conventional Ir loadings (1–2 mg cm^{-2}) [39,42]. Additional details on catalyst testing references are provided in Table S6. Furthermore, Ir/TiO_2 outperforms Ir black at lower current densities but shows lower performance at higher, which aligns with its higher ohmic resistance of Ir/TiO_2 (0.021 Ω) compared to Ir black (0.017 Ω) (Fig. 9b). This increased resistance may be attributed to the lower conductivity of the TiO_2 nanoparticles compared to unsupported Ir and IrO_x nanoparticles.

The IV curves 2 and 3 were recorded after 3 and 6 h of potential switching between 1.6 V and 1.7 V (Fig. S13), respectively. Results indicate that Ir/TiO_2 shows a slight decrease in activity, with the potential at 1 A cm^{-2} increasing from 1.56 V (IV 1) to 1.59 V (IV 2) and 1.61 V (IV 3). In contrast, Ir black remains stable, maintaining a potential of 1.62 V at 1 A cm^{-2} for both IV 2 and IV 3. On the other hand, Ir/TiN shows significantly worse activity than both Ir/TiO_2 and Ir black. This reduced performance is associated with high ohmic resistance (0.045 Ω, Fig. 9b), which further increases during the second and third IV curves. This suggests that Ir/TiN nanoparticles may have a problem maintaining the electrical conductivity across the catalyst layer under the operational conditions of the single-cell PEMWE. Interestingly, the Ir/TiC catalyst shows performance improvement, with the potential at 1 A cm^{-2} decreasing from 1.85 V (IV 1) to 1.72 V for IV 2 and IV 3, despite the worsening ohmic resistance. This counterintuitive behavior indicates the presence of a specific process that enhances Ir/TiC performance under extended operation, contrasting with the trends observed in the other samples and their results in the RDE setup. The causes of the high ohmic resistance in Ir/TiN and the degradation mechanism influencing the unexpected improvement of the Ir/TiC performance are not immediately clear, and they will be further discussed in the next section.

3.4. Post-mortem physicochemical analysis of the MEAs

Post-mortem physicochemical analysis of the MEAs was conducted to evaluate the impact of catalyst testing in PEMWE. XPS analysis of the anode side (Fig. 10) indicates complete oxidation of the catalyst surfaces. Examination of the Ti 2p core level (Fig. 10a) shows no significant variations in the Ti-O species for Ir/TiO_2 compared to the initial catalyst powder. In contrast, Ir/TiC and Ir/TiN exhibit notable changes: Ti-C species are absent in Ir/TiC, and neither Ti-N nor Ti-O_x-N_y species are detectable in Ir/TiN. Consequently, Ti 2p spectra for all samples display a doublet corresponding exclusively to the Ti-O species. Interestingly, the binding energies of Ti-O species differ across samples. For Ir/TiO_2 and Ir/TiC, the energy aligns with crystalline TiO_2 (459.0 eV); while for Ir/TiN, it shifts to 458.7 eV, characteristic of amorphous TiO_2. Saari et al. [45] conducted a comprehensive computational and experimental study on the XPS distinctions between amorphous and crystalline TiO_2, which supports our observations.

Despite these structural differences, the catalytic activities of Ir/TiN (low activity) and Ir/TiO_2 (high activity) remain counterintuitive. The amorphous TiO_2 present on the surface of Ir/TiN is known to generate oxygen vacancies that enhance the electrical conductivity [46]. However, the poor stability of amorphous TiO_2 under acidic conditions [47]

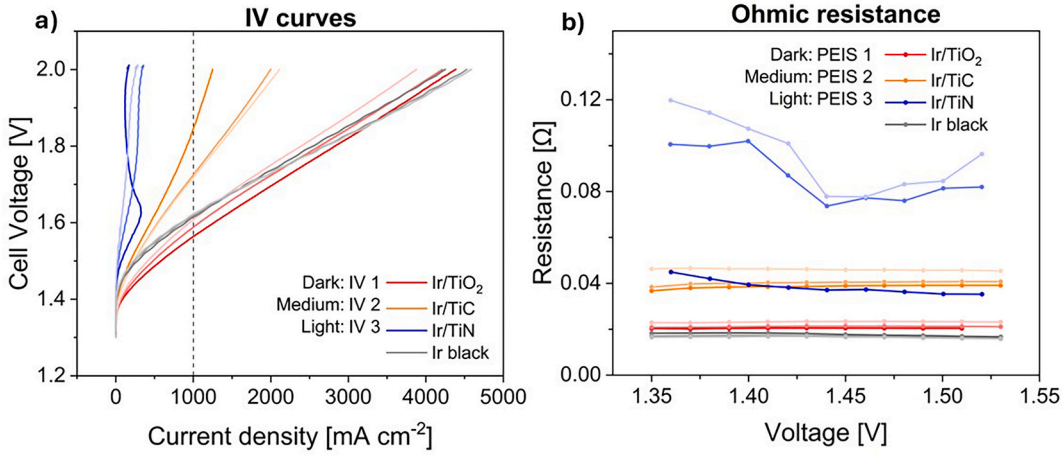

Fig. 9. IV curves (a) and ohmic resistance (b) measured for the first time (dark), second time (medium), and third time (light).

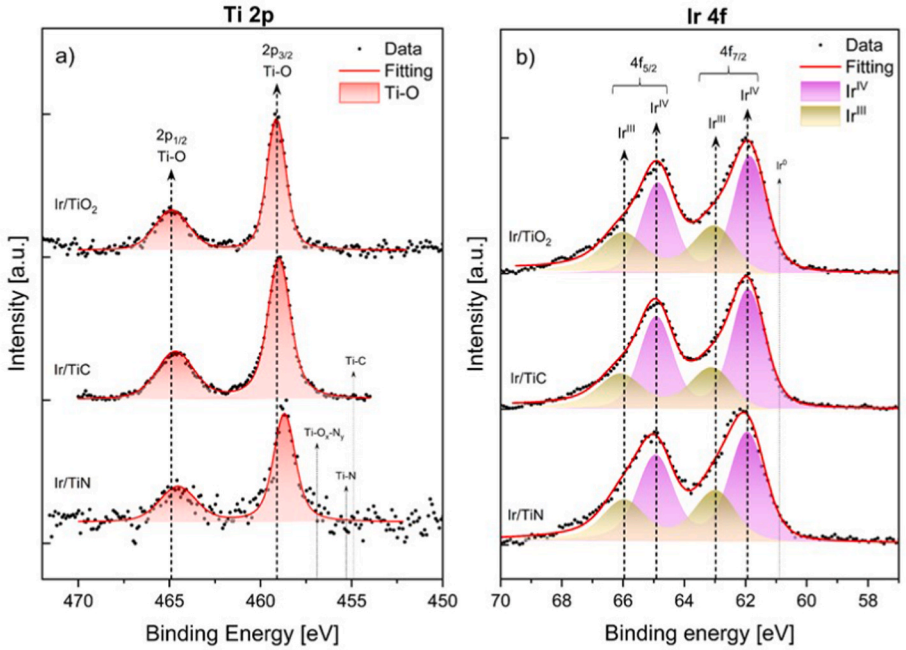

Fig. 10. XPS spectra of the anode side of the MEAs for Ir/TiO_2, Ir/TiC, and Ir/TiN, including Ti 2p core level (a) and Ir 4f core level (b).

suggests partial dissolution of the layer during the PEMWE testing. Thus, the possible benefits of the amorphous TiO_2 structure cancel and cause a significant drop in conductivity, as evidenced by the increased ohmic resistance for Ir/TiN (Fig. 9b). Furthermore, the loss of the amorphous layer weakens the Ir-TiN metal-support interaction, resulting in catalyst inhibition. In contrast, the superior stability of crystalline TiO_2 under acidic conditions [47] and the strong interaction between Ir and Ti explain the enhanced performance of Ir/TiO_2.

The Ir 4f spectra show complete oxidation for all three catalysts, with the metallic Ir^0 doublet no longer present and replaced by doublets for Ir^{IV} and Ir^{III} oxidation states. The ratio of these states is 0.60, 0.50, and 0.56 for Ir/TiO_2, Ir/TiC, and Ir/TiN, respectively, with Ir^{IV} being the predominant species. All three samples undergo oxidation, resulting in a similar surface composition for the Ti 2p and Ir 4f core levels. However, differences in the oxidation phase, linked to amorphous vs. crystalline TiO_2, play a critical role in influencing variations in the catalytic performance.

Next, XRD analysis was conducted to determine the phase composition in the bulk of the catalyst layer after PEMWE testing. In Fig. 11, the Ir/TiO_2 contains reflections of both anatase (marked with asterisks) and rutile (marked with dots) TiO_2, consistent with the initial powder samples (Fig. 3a) and remarking the already proven stability of crystalline TiO_2. For Ir/TiC, the absence of TiC diffraction peaks indicates complete oxidation of the nanoparticles, extending from the surface (as confirmed by XPS, Fig. 10) to the bulk. Peaks at 2θ of 27.4°, 36.0°, 41.2°, and 54.3° are assigned to rutile TiO_2 planes (110), (101), (111), and (211), respectively. Additionally, a weak peak at 2θ of 25.2° corresponds to the anatase TiO_2 (101) plane, and a peak at 2θ of 39.8° likely indicates platinum (111), probably detected from the cathode side of the MEA. TiC nanoparticles have previously been studied as a support for Ir thin films, showing moderate TiC oxidation due to the protective coating provided by the Ir layer [48]. In this work, however, Ir nanoparticles just partially cover the TiC surface (Fig. 1b), making TiC highly susceptible to the acidic and high-potential conditions of PEMWE. Nevertheless, the observed improvement in the catalytic performance of Ir/TiC nanoparticles after continuous potential switching (Fig. 9a) remains unexplained and will be discussed in the next section. For Ir/TiN, peaks at 2θ of 36.6° and 42.6°, corresponding to the TiN (111) and (200) planes, reveal better stability of TiN nanoparticles to the harsh

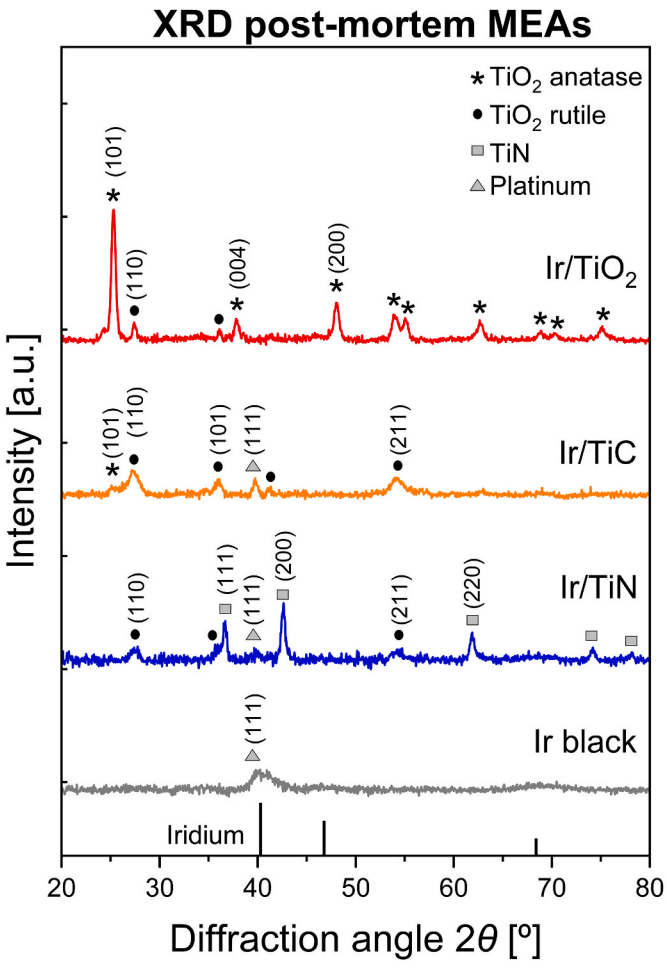

Fig. 11. XRD diffraction patterns of the MEAs for Ir/TiO_2, Ir/TiC, Ir/TiN, and Ir black. The bars on the bottom correspond to the Ir diffraction peaks.

conditions of the water electrolyzer. Rutile TiO_2 and Pt peaks, as described for Ir/TiC, are also present, though no anatase reflections are observed.

The above results indicate the partial oxidation and phase transformation of TiC and TiN into the rutile TiO_2 phase, while TiO_2 nanoparticles predominantly retain their original anatase phase. Notably, the anatase structure is characterized by a higher electrical conductivity compared to the rutile structure [49], which further explains the superior catalytic activity observed for the Ir/TiO_2 sample. The reference unsupported Ir nanoparticles show broad and low-intensity peaks at 2Θ of 40.3° and 46.8°, corresponding to Ir (111) and (200) planes. Finally, as with the initial powder samples, no distinct iridium or iridium oxide reflections are visible in the Ir/TiO_2, Ir/TiC, or Ir/TiN patterns, suggesting an amorphous or nanosized structure of the iridium crystallites.

The previous XPS and XRD analyses explain the catalytic behavior of Ir/TiO_2 and Ir/TiN nanoparticles. However, the enhancement of the catalytic activity for Ir/TiC (Fig. 9b) upon complete TiC oxidation remains inexplicable with the information collected so far. Thus, SEM and EDX measurements were performed on both the anode and cathode sides of the MEAs (Fig. 12). The Ir/Ti atomic ratios in the catalyst layers are 0.09 for Ir/TiO_2, 0.35 for Ir/TiC, and 0.09 for Ir/TiN, compared to an initial ratio of 0.08 for Ir/TiO_2 and Ir/TiC and 0.07 for Ir/TiN. These findings suggest a similar Ir-to-Ti content for Ir/TiO_2 and Ir/TiN before and after testing in PEMWE. Differently, Ir/TiC shows a fivefold increase in Ir content. This indicates the titanium dissolution consequence of the surface and bulk oxidation, as confirmed by XPS and XRD. Evidence of the TiC dissolution is further supported by the elemental mapping in Fig. 12f, which shows an inhomogeneous Ti distribution within the Ir/TiC catalyst layer in contrast with the Ti distribution in Ir/TiO_2 and Ir/TiN (Fig. 12b and j), which appears more uniform. Traces of titanium are also detected on the cathode side of the Ir/TiC (Fig. 12h), suggesting the titanium cation migration through the Nafion membrane. This migration might lead to titanium poisoning of both the cathode and the membrane, increasing the ohmic resistance throughout the MEA (Fig. 9b). Additionally, the PEIS measurements for Ir/TiC (Fig. S14d–f) reveal two distinct semicircles: a high-frequency semicircle corresponding to the ion transport (as supported by the non-exponential trend of charge transfer resistance in Fig. S16c), and a low-frequency semicircle associated with the oxygen evolution reaction at the anode. The latter shows an exponential trend in charge transfer resistance, as seen in Fig. S16d for Ir/TiC and in Fig. S16b for the other catalysts. Notably, the high-frequency semicircle is not distinguished in the PEIS spectra of Ir/TiO_2 (Fig. S14a–c), Ir/TiN (Fig. S14g–i), and Ir black (Fig. S14j–l), highlighting the specific impact of titanium dissolution and its migration through the membrane tothe cathode side. This migration may reduce proton conductivity in both the ionomer and the membrane in the Ir/TiC sample. The corresponding Randles equivalent circuit and extracted fitting parameters, such as charge transfer resistance, constant phase element (CPE), and CPE exponent (α), are presented in Fig. S15 and Fig. S16, respectively. The cation migration through polymer electrolyte membranes is a well-known phenomenon, and numerous studies have investigated the transport properties of monovalent and multivalent cations [50]. The literature suggests that membrane degradation arises from the limited proton transport, which results from the interaction between the sulfonate groups in the membrane and the migrating cations [51].

To further investigate this phenomenon, EDX analysis was performed on the cross-sections of all three MEAs (Fig. S17). The elemental mapping in Fig. 13 shows that Ti intensity concentrates at the anode in Ir/TiO_2 (Fig. 13b) and Ir/TiN (Fig. 13f), indicating better titanium stability. In contrast, Ir/TiC (Fig. 13d) exhibits a non-uniform Ti distribution, with a gradient extending from the anode to the cathode, supporting the hypothesis of Ti cation migration.

Although degradation of the Ti-based support nanoparticles in Ir-based catalysts is undesirable, in the case of Ir/TiC, the oxidation and dissolution of the TiC nanoparticles enhance the contact between Ir nanoparticles. This effect contributes to the improvement of the catalytic performance of Ir/TiC over time, as observed in Fig. 9a. A long-term stability test would provide more insight into the consequences of TiC dissolution and migration on the catalytic performance of Ir/TiC nanoparticles. Nonetheless, addressing this issue exceeds the intended objectives of this study. Additional elemental mapping information for Ir

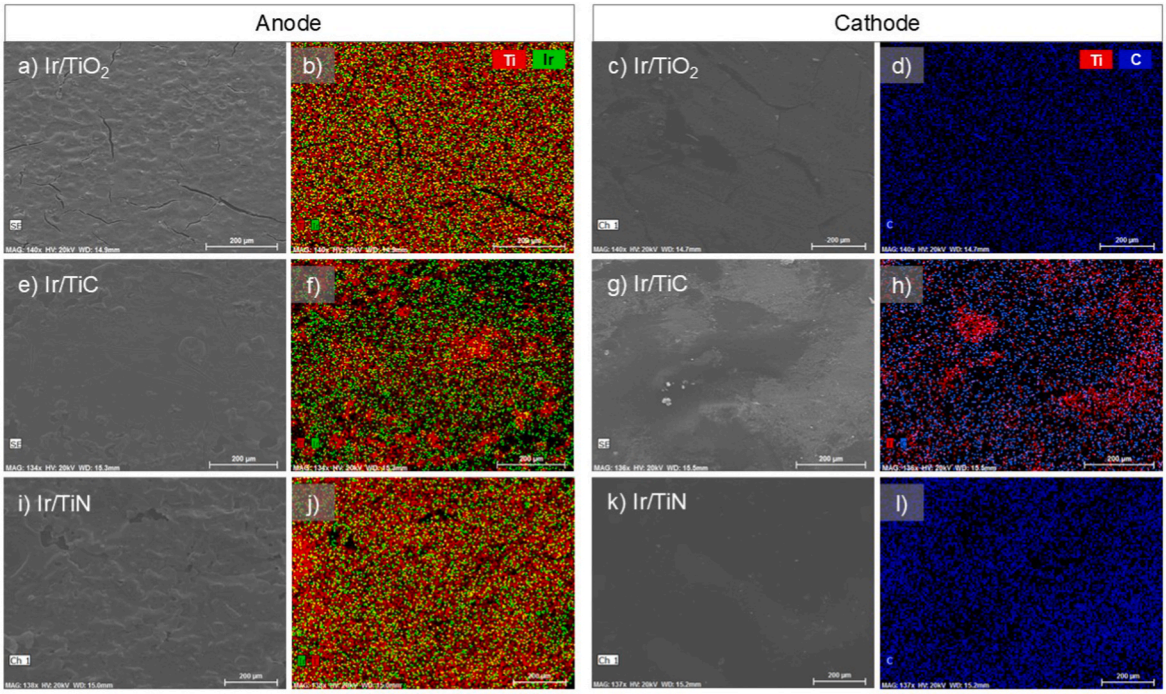

Fig. 12. SEM micrographs and their corresponding EDX mapping for the anode (left) and cathode (right) sides of the Ir/TiO_2 (a–d), Ir/TiC (e–h), and Ir/TiN (i–l) MEAs. Color code: red (titanium), green (iridium), and blue (carbon). (For interpretation of the references to color in this figure legend, the reader is referred to the Web version of this article.)

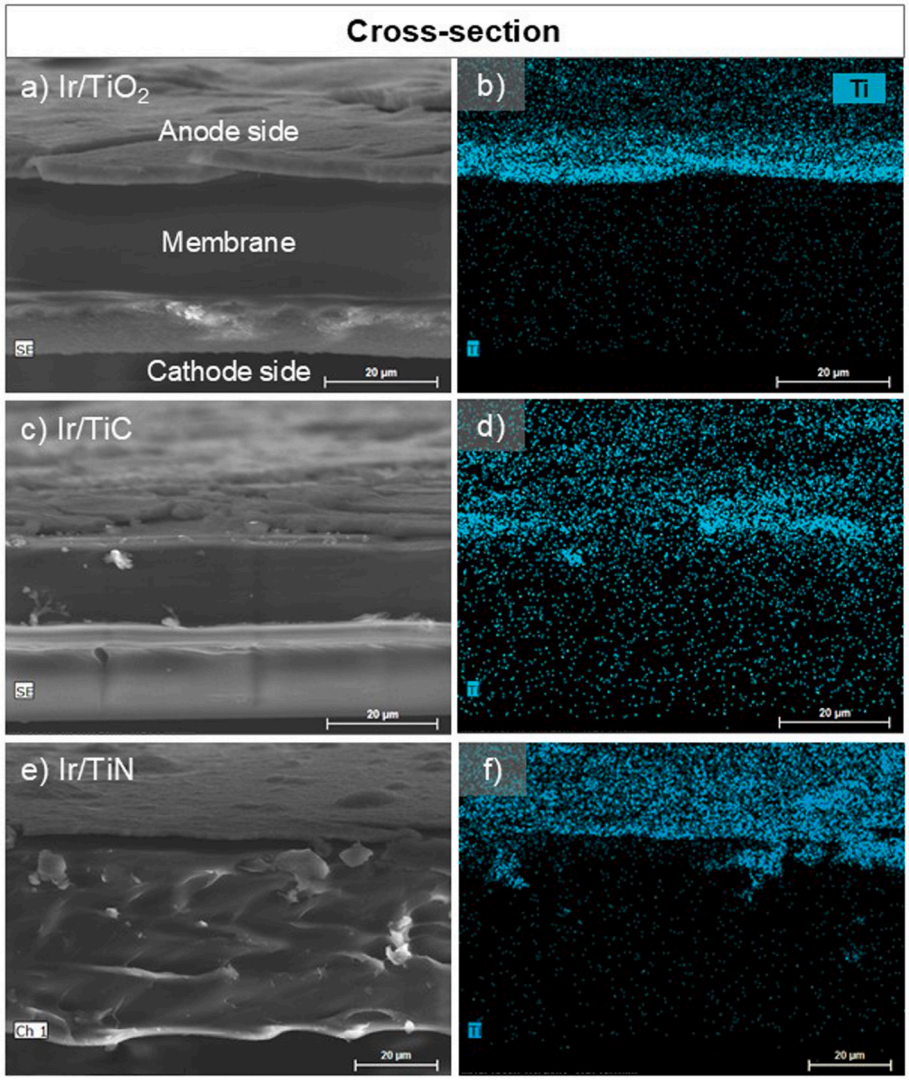

Fig. 13. SEM micrographs of the MEAs cross-section for Ir/TiO_2 (a), Ir/TiC (c), and Ir/TiN (d), and their respective EDX mapping (b, d, f). Color code: blue (titanium). (For interpretation of the references to color in this figure legend, the reader is referred to the Web version of this article.)

and F is provided in Fig. S18.

4. Conclusions

Developing efficient and stable catalysts for the oxygen evolution reaction (OER) in water electrolyzers, while minimizing iridium loading, is essential for sustainable hydrogen production. This study systematically explored the impact of titanium-based supports on the morphology, chemical structure, conductivity, OER performance, and stability of iridium catalysts in both half- and single electrochemical cells. A series of Ir nanoparticles (~1.7 nm) were synthesized onto TiO_2, TiC, and TiN nanoparticles, showing a uniform distribution. The conductivity of the supports plays a significant role in determining electrochemical performance. High-conductivity supports like TiC facilitate efficient charge transfer, resulting in a higher density of electrochemically active sites and greater H_{upd} peak intensity compared with low-conductivity TiO_2. However, conductivity alone does not guarantee better catalytic performance, as demonstrated by the superior stability and activity of Ir/TiO_2 under real operating conditions of the PEM water electrolyzer. Ir/TiO_2 outperformed all other supported samples in both *ex-situ* RDE (overpotential of 260 mV at 10 mA cm^{-2}) and *in-situ* PEMWE (potential of 1.56 V at 1 A cm^{-2}) setups, showing activity and stability comparable to unsupported Ir black (overpotential of 253 mV at 10 mA cm^{-2} in RDE and potential of 1.61 V at 1 A cm^{-2} in PEMWE). This performance is attributed to the stability of crystalline anatase TiO_2, which resists oxidation and dissolution under acidic conditions, ensuring robust metal-support interactions and consistent electrochemical activity. In contrast, TiC underwent complete oxidation during electrolyzer operation, leading to titanium cation migration that poisoned the membrane and degraded the catalyst layer. Although this sacrificial degradation temporarily enhanced Ir contact and activity, it might compromise long-term stability. TiN nanoparticles, on the other hand, suffered from an unstable amorphous oxide/oxynitride surface layer under acidic conditions, preventing effective Ir anchoring and causing rapid catalyst deactivation. These findings underscore the critical importance of support material structure, providing valuable insights into advanced catalyst design for highly active and stable OER systems in water electrolyzers.

CRediT authorship contribution statement

Lucinda Blanco-Redondo: Writing – original draft, Methodology, Investigation, Formal analysis, Data curation, Conceptualization. **Yevheniia Lobko:** Writing – review & editing, Validation, Supervision, Methodology, Investigation, Formal analysis, Conceptualization. **Alina Madalina Darabut:** Writing – review & editing, Data curation.

Jaroslava Nováková: Writing – review & editing, Data curation. **Thu Ngan Dinhová:** Writing – review & editing, Data curation. **Maryna Vorokhta:** Writing – review & editing, Data curation. **Miquel Gamón Rodríguez:** Writing – review & editing, Data curation. **Milan Dopita:** Writing – review & editing, Formal analysis, Data curation. **Michal Mazur:** Writing – review & editing, Data curation. **Jakub Hraníček:** Writing – review & editing, Formal analysis, Data curation. **Yurii Yakovlev:** Writing – review & editing, Investigation. **Tomáš Hrbek:** Writing – review & editing, Methodology, Formal analysis, Data curation. **Vladimír Matolín:** Writing – review & editing. **Iva Matolínová:** Writing – review & editing, Validation.

Declaration of competing interest

The authors declare that they have no known competing financial interests or personal relationships that could have appeared to influence the work reported in this paper.

Acknowledgements

The authors acknowledge financial support from the European Regional Development Fund (ERDF) and the European Social Fund Plus (ESF+), under the Programme Johannes Amos Comenius (OP JAK), project The Energy Conversion and Storage (CZ.02.01.01/00/22_008/0004617). Michal Mazur acknowledges funding from the European Structural and Investment Funds, Operational Programme Research, Development and Education (OP VVV), project Excellent Research Teams (CZ.02.1.01/0.0/0.0/15_003/0000417-CUCAM).

Appendix B. Supplementary data

Supplementary data to this article can be found online at https://doi.org/10.1016/j.renene.2025.124295.

Data availability

Data will be available in the repository on Zenodo DOI 0.5281/zenodo.14545132.

References

[1] International Energy Agency, Net Zero by 2050 - a Roadmap for the Global Energy Sector, 2021. www.iea.org/t&c/.
[2] C. Fu, T. O'Carroll, S. Shen, L. Luo, J. Zhang, H. Xu, G. Wu, Metallic-Ir-based anode catalysts in PEM water electrolyzers : achievements, challenges, and perspectives, Curr. Opin. Electrochem. 38 (2023) 1–9, https://doi.org/10.1016/j.coelec.2023.101227.
[3] DOE technical targets for proton exchange membrane electrolysis, (n.d.). https://www.energy.gov/eere/fuelcells/technical-targets-proton-exchange-membrane-electrolysis (accessed March 28, 2023).
[4] H. Li, Y. Pan, L. Wu, R. He, Z. Qin, S. Luo, L. Yang, J. Zeng, IrO2 deposited on RuO2 as core-shell structured RuO2@IrO2 for oxygen evolution reaction in electrochemical water electrolyzer, Mol. Catal. 551 (2023), https://doi.org/10.1016/j.mcat.2023.113619.
[5] S.H. Ahn, D. Jin, C. Lee, Y. Lee, Oxygen-vacancy rich IrxMo1−xOy nanofibers for oxygen evolution reaction: excellent pH-universal and electrolyte-concentration-independent catalytic activity, J Mater Chem A Mater 11 (2023) 14941–14951, https://doi.org/10.1039/d3ta01614e.
[6] Z. Kang, G. Yang, J. Mo, Development of an ultra-thin electrode for the oxygen evolution reaction in proton exchange membrane water electrolyzers, Renew. Energy 224 (2024), https://doi.org/10.1016/j.renene.2024.120159.
[7] Y. Liu, Y. Chen, X. Mu, Z. Wu, X. Jin, J. Li, Y. Xu, L. Yang, X. Xi, H. Jang, Z. Lei, Q. Liu, S. Jiao, P. Yan, X. Li, R. Cao, Spinel-anchored iridium single atoms enable efficient acidic water oxidation via intermediate stabilization effect, ACS Catal. 13 (2023) 3757–3767, https://doi.org/10.1021/acscatal.2c05940.
[8] L. Moriau, M. Smiljanić, A. Lončar, N. Hodnik, Supported iridium-based oxygen evolution reaction electrocatalysts - recent developments, ChemCatChem 14 (2022), https://doi.org/10.1002/cctc.202200586.
[9] P. Mazúr, J. Polonský, M. Paidar, K. Bouzek, Non-conductive TiO2 as the anode catalyst support for PEM water electrolysis, Int. J. Hydrogen Energy 37 (2012) 12081–12088, https://doi.org/10.1016/j.ijhydene.2012.05.129.
[10] D. Bae, B. Seger, P.C.K. Vesborg, O. Hansen, I. Chorkendorff, Strategies for stable water splitting via protected photoelectrodes, Chem. Soc. Rev. 46 (2017) 1933–1954, https://doi.org/10.1039/C6CS00918B.
[11] Y. Qin, Y. Wang, R. Wen, L. Wang, M. Dou, F. Wang, Interface-engineering strategy for boosting low-Ir catalytic water oxidation using a conductive Ti4O7 support, ACS Catal. (2024) 13915–13926, https://doi.org/10.1021/acscatal.4c03862.
[12] Y. Lin, B. Wu, A. Chen, J. Su, L. Chen, Iridium-titanium oxides for efficient oxygen evolution reaction in acidic media, Int. J. Hydrogen Energy 48 (2023) 10368–10376, https://doi.org/10.1016/j.ijhydene.2022.11.348.
[13] W. Hu, S. Chen, Q. Xia, IrO2/Nb-TiO2 electrocatalyst for oxygen evolution reaction in acidic medium, Int. J. Hydrogen Energy 39 (2014) 6967–6976, https://doi.org/10.1016/j.ijhydene.2014.02.114.
[14] S. Zhao, A. Stocks, B. Rasimick, K. More, H. Xu, Highly active, durable dispersed iridium nanocatalysts for PEM water electrolyzers, J. Electrochem. Soc. 165 (2018) F82–F89, https://doi.org/10.1149/2.0981802jes.
[15] S.B. Han, Y.H. Mo, Y.S. Lee, S.G. Lee, D.H. Park, K.W. Park, Mesoporous iridium oxide/Sb-doped SnO2 nanostructured electrodes for polymer electrolyte membrane water electrolysis, Int. J. Hydrogen Energy 45 (2020) 1409–1416, https://doi.org/10.1016/j.ijhydene.2019.11.109.
[16] E.J. Kim, K. hyun Kim, J. Bak, K.H. Lee, E.A. Cho, Carbon nanotube-titanium dioxide nanocomposite support for improved activity and stability of an iridium catalyst toward the oxygen evolution reaction, RSC Adv. 12 (2022) 35943–35949, https://doi.org/10.1039/d2ra05027g.
[17] X. Wu, B. Feng, W. Li, Y. Niu, Y. Yu, S. Lu, C. Zhong, P. Liu, Z. Tian, L. Chen, W. Hu, C.M. Li, Metal-support interaction boosted electrocatalysis of ultrasmall iridium nanoparticles supported on nitrogen doped graphene for highly efficient water electrolysis in acidic and alkaline media, Nano Energy 62 (2019) 117–126, https://doi.org/10.1016/j.nanoen.2019.05.034.
[18] Y.C. Kimmel, X. Xu, W. Yu, X. Yang, J.G. Chen, Trends in electrochemical stability of transition metal carbides and their potential use as supports for low-cost electrocatalysts, ACS Catal. 4 (2014) 1558–1562, https://doi.org/10.1021/cs500182h.
[19] G. Li, K. Li, L. Yang, J. Chang, R. Ma, Z. Wu, J. Ge, Boosted Performance of Ir Species by Employing Tin as the Support Toward Oxygen Evolution Reaction, vol. 18, 2018, https://doi.org/10.1021/acsami.8b14172.
[20] M. Bele, K. Stojanovski, P. Jovanovič, L. Moriau, G. Koderman Podboršek, J. Moškon, P. Umek, M. Sluban, G. Dražič, N. Hodnik, M. Gaberšček, Towards stable and conductive titanium oxynitride high-surface-area support for iridium nanoparticles as oxygen evolution reaction electrocatalyst, ChemCatChem 11 (2019) 5038–5044, https://doi.org/10.1002/cctc.201901487.
[21] L. Blanco-Redondo, Y. Lobko, K. Veltruská, J. Nováková, M. Mazur, A.M. Darabut, T. Hrbek, M. Dopita, J. Hraníek, Y. Yakovlev, I. Matolínová, V. Matolín, Bifunctional Pt-Ir nanoparticle catalysts for oxygen reduction and evolution reactions: investigating the influence of surface composition on the catalytic properties, Sustain. Energy Fuels 8 (2024) 797–810, https://doi.org/10.1039/d3se01238g.
[22] F. Scarpelli, T.F. Mastropietro, T. Poerio, N. Godbert, Mesoporous TiO2 thin films: state of the art, in: Titanium Dioxide - Material for a Sustainable Environment, InTech, 2018, pp. 57–80, https://doi.org/10.5772/intechopen.74244.
[23] Y. Zhang, Z. Zhang, X. Yang, R. Wang, H. Duan, Z. Shen, L. Li, Y. Su, R. Yang, Y. Zhang, X. Su, Y. Huang, T. Zhang, Tuning selectivity of CO_2 hydrogenation by modulating the strong metal-support interaction over Ir/TiO_2 catalysts, Green Chem. 22 (2020) 6855–6861, https://doi.org/10.1039/d0gc02302g.
[24] E.N. El Sawy, H.T. Handal, V. Thangadurai, V.I. Birss, PtxIry alloy nanoparticles with fully tunable bulk and surface compositions, J. Mater. Chem. 4 (2016) 15400–15410, https://doi.org/10.1039/c6ta06161c.
[25] J.F. Moulder, W.F. Stickle, P.E. Sobol, Handbook of X-ray Photoelectron Spectroscopy, Perkin-Elmer Corporation, Minnesota, 1992.
[26] P. Krishnan, M. Liu, P.A. Itty, Z. Liu, V. Rheinheimer, M.H. Zhang, P.J.M. Monteiro, L.E. Yu, Characterization of photocatalytic TiO2 powder under varied environments using near ambient pressure X-ray photoelectron spectroscopy, Sci. Rep. 7 (2017), https://doi.org/10.1038/srep43298.
[27] S. Köstlmeier, C. Elsässer, Density functional study of the "titanium effect" at metal-ceramic interfaces, J. Phys. Condens. Matter 12 (2000) 1209–1222.
[28] G. Koderman Podborsek, L. Suhadolnik, A. Loncar, M. Bele, A. Hrnjic, Z. Marinko, J. Kovac, A. Kokalj, L. Gasparic, A.K. Surca, A.R. Kamsek, G. Drazic, M. Gaberscek, N. Hodnik, P. Jovanovic, Iridium stabilizes ceramic titanium oxynitride support for oxygen evolution reaction, ACS Catal. 12 (2022) 15135–15145, https://doi.org/10.1021/acscatal.2c04160.
[29] H. Belhadj, I. Moulefera, L. Sabantina, A. Benyoucef, Effects of incorporating titanium dioxide with titanium Carbide on hybrid materials reinforced with polyaniline: synthesis, characterization, electrochemical and supercapacitive properties, Fibers 10 (2022), https://doi.org/10.3390/fib10050046.
[30] W.J.F. Gannon, D.R. Jones, C.W. Dunnill, Enhanced lifetime cathode for alkaline electrolysis using standard commercial titanium nitride coatings, Processes 7 (2019), https://doi.org/10.3390/pr7020112.
[31] N.C. Saha, H.G. Tompkins, Titanium nitride oxidation chemistry: an x-ray photoelectron spectroscopy study, J. Appl. Phys. 72 (1992) 3072–3079, https://doi.org/10.1063/1.351465.
[32] D. Reyes-Coronado, G. Rodriguez-Gattorno, M. Espinosa-Pesqueira, J.M. Gardner, G.J. Meyer, G. Oskam, Synthesis and characterization of TiO2 nanoparticles: anatase, brookite, and rutile, Solar Hydrogen and Nanotechnology II (2007) 66500X, https://doi.org/10.1117/12.732647. SPIE.
[33] D.A.J. Rand, R. Woods, Cyclic voltammetric studies on iridium electrodes in sulphuric acid solutions, Electroanalytical Chemistry and Interfacial Electrochemistry 55 (1974) 375–381.

[34] J.C. François, Y. Massiani, P. Gravier, Characterization and optical properties of thin films formed on TiN coating during electrochemical treatments, Thin Solid Films 223 (1993) 223–229.
[35] P. Nayak, R.C. Xie, R.G. Palgrave, R.G. Compton, Electro-oxidation of titanium carbide nanoparticles in aqueous acid creates TiC@TiO_2 core-shell structures, Chemelectrochem 8 (2021) 911–917, https://doi.org/10.1002/celc.202001498.
[36] X. Han, T. Mou, A. Islam, S. Kang, Q. Chang, Z. Xie, X. Zhao, K. Sasaki, J. A. Rodriguez, P. Liu, J.G. Chen, Theoretical prediction and experimental verification of IrOx supported on titanium nitride for acidic oxygen evolution reaction, J. Am. Chem. Soc. 146 (2024) 16499–16510, https://doi.org/10.1021/jacs.4c02936.
[37] S.S. Karade, R. Sharma, S. Gyergyek, P. Morgen, S.M. Andersen, IrO_2/Ir composite nanoparticles (IrO2@Ir) supported on TiNxOy coated TiN: efficient and robust oxygen evolution reaction catalyst for water electrolysis, ChemCatChem 15 (2023), https://doi.org/10.1002/cctc.202201470.
[38] C.T.K. Nguyen, N.Q. Tran, T.A. Le, H. Lee, Covalently bonded Ir(IV) on conducted blue TiO2 for efficient electrocatalytic oxygen evolution reaction in acid media, Catalysts 11 (2021), https://doi.org/10.3390/catal11101176.
[39] J.I. Cha, C. Baik, S.W. Lee, C. Pak, Improved utilization of IrOx on Ti4O7 supports in membrane electrode assembly for polymer electrolyte membrane water electrolyzer, Catal. Today 403 (2022) 19–27, https://doi.org/10.1016/j.cattod.2022.01.015.
[40] S. Sui, L. Ma, Y. Zhai, TiC supported Pt-Ir electrocatalyst prepared by a plasma process for the oxygen electrode in unitized regenerative fuel cells, J. Power Sources 196 (2011) 5416–5422, https://doi.org/10.1016/j.jpowsour.2011.02.058.
[41] K. Zhang, W. Mai, J. Li, H. Wang, G. Li, W. Hu, Highly scattered Ir oxides on TiN as an efficient oxygen evolution reaction electrocatalyst in acidic media, J. Mater. Sci. 55 (2020) 3507–3520, https://doi.org/10.1007/s10853-019-04201-4.
[42] D. Böhm, M. Beetz, C. Gebauer, M. Bernt, J. Schröter, M. Kornherr, F. Zoller, T. Bein, D. Fattakhova-Rohlfing, Highly conductive titania supported iridium oxide nanoparticles with low overall iridium density as OER catalyst for large-scale PEM electrolysis, Appl. Mater. Today 24 (2021) 101134, https://doi.org/10.1016/j.apmt.2021.101134.
[43] C. Van Pham, M. Bühler, J. Knöppel, M. Bierling, D. Seeberger, D. Escalera-López, K.J.J. Mayrhofer, S. Cherevko, S. Thiele, IrO_2 coated TiO_2 core-shell microparticles advance performance of low loading proton exchange membrane water electrolyzers, Appl. Catal., B 269 (2020) 118762, https://doi.org/10.1016/j.apcatb.2020.118762.
[44] L. Ma, S. Sui, Y. Zhai, Preparation and characterization of Ir/TiC catalyst for oxygen evolution, J. Power Sources 177 (2008) 470–477, https://doi.org/10.1016/j.jpowsour.2007.11.106.
[45] J. Saari, H. Ali-Löytty, K. Lahtonen, M. Hannula, L. Palmolahti, A. Tukiainen, M. Valden, Low-temperature route to direct amorphous to rutile crystallization of TiO2 thin films grown by atomic layer deposition, J. Phys. Chem. C 126 (2022) 15357–15366, https://doi.org/10.1021/acs.jpcc.2c04905.
[46] N.A. Deskins, J. Du, P. Rao, The structural and electronic properties of reduced amorphous titania, Phys. Chem. Chem. Phys. 19 (2017) 18671–18684, https://doi.org/10.1039/c7cp02940c.
[47] G.C. Correa, B. Bao, N.C. Strandwitz, Chemical stability of titania and alumina thin films formed by atomic layer deposition, ACS Appl. Mater. Interfaces 7 (2015) 14816–14821, https://doi.org/10.1021/acsami.5b03278.
[48] J. Zhang, X. Cao, Y.F. Jiang, S.F. Hung, W. Liu, H. Bin Yang, C.Q. Xu, D.S. Li, T. Zhang, Y. Li, J. Li, B. Liu, Surface enrichment of Ir on the IrRu alloy for efficient and stable water oxidation catalysis in acid, Chem. Sci. 13 (2022) 12114–12121, https://doi.org/10.1039/d2sc03947h.
[49] A. Soussi, A. Ait Hssi, M. Boujnah, L. Boulkadat, K. Abouabassi, A. Asbayou, A. Elfanaoui, R. Markazi, A. Ihlal, K. Bouabid, Electronic and optical properties of TiO2 thin films: combined experimental and theoretical study, J. Electron. Mater. 50 (2021) 4497–4510, https://doi.org/10.1007/s11664-021-08976-8.
[50] A. Paspureddi, Z. Zhang, V. Ganesan, M.M. Sharma, L.E. Katz, Mechanism of monovalent and divalent ion mobility in Nafion membrane: an atomistic simulation study, J. Chem. Phys. 158 (2023), https://doi.org/10.1063/5.0145205.
[51] R. Cui, Z. Zhang, Y. Wang, F. Liu, H. Wang, C. Bi, C. Yu, Y. Zhou, Effect of cations (Na+, Co2+, Fe3+) contamination in Nafion membrane: a molecular simulations study, Int. J. Hydrogen Energy 50 (2024) 635–649, https://doi.org/10.1016/j.ijhydene.2023.09.295.